The coalescence speed of a pendent and a sessile drop

By S. T. THORODDSEN[1], K. TAKEHARA[2] AND T. G. ETOH[2]

[1]Mechanical Engineering, National University of Singapore, 9 Engineering Drive 1, Singapore 117576

[2]Civil and Environmental Engineering, Kinki University, Higashi-Osaka 577-8502, Japan

When two liquid drops come into contact, they coalesce rapidly, owing to the large curvature and unbalanced surface-tension forces in the neck region. We use an ultra-high-speed video camera to study the coalescence of a pendent and a sessile drop, over a range of drop sizes and liquid viscosities. For low viscosity, the outward motion of the liquid contact region is successfully described by a dynamic capillary-inertial model based on the local vertical spacing between the two drop surfaces. This model applies even when the drops are of different sizes. Increasing viscosity slows down the coalescence when the Reynolds number $Re_v = \rho R_{ave} \sigma / \mu^2 < 5000$, where R_{ave} is the average of the tip radii of the two similar size drops, ρ is the liquid density, σ is the surface tension and μ the dynamic viscosity. At $Re_v \simeq 50$, the growth-rate of the neck radius has reduced by a half, which for water corresponds to a drop diameter of only $2\,\mu m$. For the largest viscosities, the neck region initially grows in size at a constant velocity. The neck curvature also becomes progressively sharper with increasing viscosity. The results are compared to previously predicted power laws, finding slight, but significant deviations from the predicted exponents. These deviations are most probably caused by the finite initial contact radius.

1. Introduction

There has recently been considerable interest in the two basic 'singularities' occurring in free-surface flows, i.e. the breakup of a liquid thread into two pieces and the merging or coalescence of two liquid masses. The pinch-off of a drop and the breakup of a liquid thread has been extensively studied, as reviewed by Eggers (1997). This has, for example, revealed an extraordinary pinch-off cascade by Shi, Brenner & Nagel (1994).

However, as Eggers (1997) points out, the temporal resolution of previous measurements has been 'insufficient to observe much of the extremely rapid motion after two surfaces touch'. To accomplish such measurements, we use herein a novel ultra-high-speed video camera, developed by Etoh *et al.* (2002, 2003) and capable of acquiring 103 consecutive frames at frame-rates up to 1 million frames s^{-1}.

The only previous measurements capable of resolving the original motions were obtained by Menchaca-Rocha *et al.* (2001) using two mercury drops sitting on a glass plate. They used a high-speed film camera capable of taking 8 consecutive frames.

Our experimental set-up focuses on the initial coalescence motions, by growing a pendent and a sessile drop on vertically aligned metal tubes, until they come into contact (see figure 1). This set-up does not therefore allow us to study the longterm evolution of coalescing drops, such as the coalescence cascade recently discovered
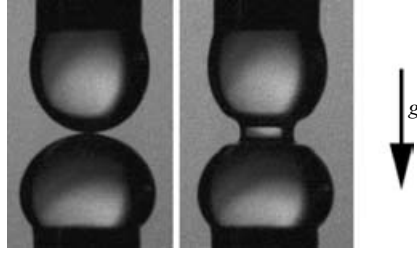
FIGURE 1. The drop orientation used in this study. Coalescence of water drops. The tube diameters are $D = 2.95\,\text{mm}$ and the radii of curvature at the contact point are $R_t = 1.53\,\text{mm}$ and $R_b = 2.05\,\text{mm}$. The second image is taken about $950\,\mu\text{s}$ after the first contact between the two drops. The frame rate was $100\,\text{kHz}$.

by Thoroddsen & Takehara (2000), for a drop coalescing with a flat liquid surface. This cascade proceeds at the capillary-inertial time scaling, with a daughter drop being pinched off at the top of the original drop. A similar cascade for a drop at an immiscible liquid–liquid interface, was previously discovered by Charles & Mason (1960).

Theoretical treatment of coalescence has mostly focused on the two-dimensional configuration. Keller, Milewski & Vanden-Broeck (2000) have computed the coalescence shapes for two-dimensional inviscid wedges, based on the self-similar solutions for capillary-driven flows, first presented by Keller & Miksis (1983). These self-similar solutions cannot be directly applied here, as our configuration has imposed external length-scales of the drop diameters. Oguz & Prosperetti (1989) have simulated the coalescence of two flat surfaces connected at a neck region. Their calculations are inviscid and were performed in both two- and three-dimensions. They have shown the formation of bubble rings when the top drop is moving downwards.

Miksis & Vanden-Broeck (1999) have found the corresponding self-similar solution for viscous wedges, over a limited range of viscosity ratios between the inner and outer liquids. The coalescence of very viscous liquid drops, where inertia is negligible, has been widely studied owing to its importance to sintering (see Martinez-Herrera & Derby 1995) and coarsening of emulsions (Rother, Zinchenko & Davis 1997). The coalescence of nano-particles such as gold is a recent topic of interest and fluid models may be of relevance here (Lee, Mori & Yasuda 2002).

Hopper (1990, 1992, 1993a, b) has found an analytical solution for the coalescence of two viscous cylinders. The solution is two-dimensional, but allows for different radii for the two cylinders. Richardson (1992) has further elucidated this solution.

Eggers, Lister & Stone (1999) have studied the asymptotics of the viscous-dominated coalescence, where the three-dimensional problem can be treated as if it were two-dimensional. Their work is formulated for the very early stages of the coalescence. They also present a dimensional argument for the inviscid case, as will be discussed in a later section.

Duchemin, Eggers & Josserand (2003) have performed inviscid simulations of this set-up, for the very early coalescence. They find repeated reconnections entrapping toroidal regions of outer fluid, when $r/R < 0.035$. This is qualitatively similar to the numerical results by Oguz & Prosperetti (1989) for two approaching surfaces.

The inverted problem, of the coalescence of two bubbles, has been studied using a linear array of high-speed photodiodes by Stover, Tobias & Denn (1997).

Measurements of the coalescence of drops in micro-devices have been carried out by Wu *et al.* (2003) and reported in more detail by Wu *et al.* (2004).

2. Experimental set-up

The orientation of the pendent and sessile drops is shown in figure 1. This set-up retains the axisymmetry around the coalescence axis, but the shapes of the two drops are distorted differently by gravity. The two drops are therefore of slightly different curvature and internal pressure. In order to find the true tip curvatures for the two drops and the vertical separations of the liquid surfaces, we have therefore used the exact static drop shapes in the coalescence model, as detailed in § 3.

2.1. *Ultra-high-speed video camera and long-distance microscope*

To capture the very rapid motions following the liquid contact, we use a novel ultra-high-speed video camera developed by Etoh *et al.* (2002, 2003) which reaches frame rates as high as 1 million frames s^{-1}. To achieve these very rapid frame rates, the camera uses in-situ image storage (ISIS) inside every pixel on the CCD chip. The prototype can store 103 consecutive frames, where each frame has 260×312 pixel elements irrespective of the frame rate used. Furthermore, a 10-bit intensity resolution generates high image quality. The ISIS structure of the prototype can, in principle, be extended to 50 Mega-frames s^{-1} using a single sensor.

This new camera records frames continually into the ISIS memory, which clears through a drain, until a trigger signal stops the imaging. This signal can therefore be timed at any of the 103 images, giving the required flexibility to the external trigger. This feature effectively allows observations of events occurring before the trigger. The movie clips are then rapidly stored onto a dedicated computer.

One of the greatest advantages of this novel video camera is its ease of use. By eliminating the need for video tapes or film developing, we can perform numerous experiments in rapid succession, thus investigating many experimental conditions in a short time. This makes the study of complex phenomena more practical than previously possible.

The diameter of the initial contact region of the two drops is of the order of $100\,\mu$m. To capture the initial motions accurately, large magnifications are therefore required. Here, we use a long-distance microscopic lens (Questar QM100). It has optical resolution of $1\,\mu$m. The experiments used magnifications in the range from 5–10, at a distance of about 15 cm.

The liquid shapes were visualized as a silhouette against an illuminated 'screen'. Diffuse backlighting is produced by one or two high-intensity spot-lights (Olympus, LG-PS2), which were shone onto a sheet of white paper or drafting paper depending on the illumination intensity required. These are cool spot-lights which were blocked between the actual video acquisitions, therefore giving minimum direct heating of the liquids. The need for high-intensity hot lamps has been troublesome for earlier high-speed camera studies of free surface flows, as they can induce thermocapillary convection. The high sensitivity of the new CCD sensor avoids any such problems, without the need for an image intensifier. The camera has Peltier cooling to reduce thermal noise, keeping the sensor temperature at around $8\,°$C. Dark regions visible in the corners of some of the video frames, e.g. figure 14, are simply due to the edges of the field of view of the lenses used.
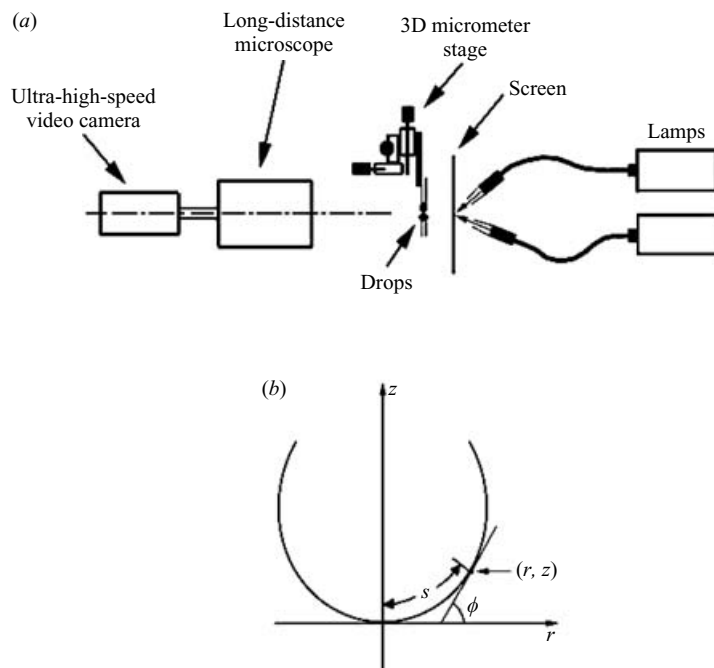
FIGURE 2. Experimental set-up. (*a*) Ultra-high-speed video camera and long-distance micro-scope, along with 3 micro-meter stages and the illuminating lamps. (*b*) Set-up sketch for the calculation of static drop shapes.

2.2. *The drop set-up*

Figure 2(*a*) shows the needle set-up used to bring the two drops into contact. Three micro-meters were used to adjust the relative position of the top needle, both to adjust the vertical spacing, and for horizontal centring of the two drops.

One of the aims of this study was to investigate the effects of drop size on the co-alescence speed. This was accomplished using different nozzle diameters D. However, practical factors limit the range of drop sizes we can study. The largest drops are excessively distorted by gravity and the smallest ones limited by the optical resolution of our system and the smallest needles available to us.

Three sets of metallic needles were used in most of the experiments herein. Their outer diameters D were 1.09, 1.78 and 2.95 mm. In a few cases, the openings of larger plastic gate valves, with outer diameters of 5.5 and 8 mm, were used. Coalescence of drops having different curvatures was also studied, as well as drops coalescing with flat liquid surfaces.

The liquids used were primarily deionized water, as well as mixtures of glycerin and water, used to vary the liquid viscosity. Similarly, limited experiments were performed with alcohol/water solutions to vary the surface tension. A small amount of salt, around 1 g/l000 ml, was added to the liquids to make them conductive. This was required for the trigger, which marked the electrical contact of the two liquid surfaces.

The drops do not touch at a point, but along a finite ring, having a diameter of the order of 100 μm. The most likely explanation is the presence of air, as has been studied, among others, by Jones & Wilson (1978) and Rother *et al.* (1997). No matter how slowly the two surfaces meet, the lubrication pressure will eventually become

strong enough to overcome the capillary pressure and deform the drops. This will most probably trap a tiny air bubble at the centre of the contact, as is observed experimentally for impacting drops, see Peck & Sigurdson (1994) and Thoroddsen, Etoh & Takehara (2003). The speed at which the two surfaces approach is here kept extremely low, of the order of $< 100\,\mu\mathrm{m\,s^{-1}}$, but could not be independently controlled. Usually, the bottom drop was grown to the centre of the image and then the top drop allowed to grow slowly until the two touched, starting the coalescence process. The gravity-driven flow of the liquids was controlled with plastic gate-valves, which were adjusted to very low flow rates, but could not be set to a specific value for this flow rate. An additional set of valves would stop and start the flow. As the needles are usually out of view of the camera, there was no direct control over where the drops meet. In general, therefore, they do not meet exactly at the midpoint between the two needles.

2.3. *Onset of motion and the electrical trigger*

In the present experiments, we use electrical contact between the two liquid surfaces to start the image sequence of each movie clip. The start of motion is observed about 20–60 μs after the electrical contact. This suggests that electrical contact is initiated just before a liquid bridge is formed between the two liquid masses. This delay appears shorter for the smallest drops, i.e. for higher curvature of the two surfaces. This suggests that surface charge may play some role in the initial electrical contact. The trigger was designed for fast response and at the same time minimizing the electrical current between the drops following the contact. We estimate this current to be less than 25 μA. The experiments of Menchaca-Rocha *et al.* (2001) with mercury drops show similar time delays. This unknown delay will certainly sabotage any attempts to construct power laws close to the initial start of motion, as t_o is unknown. This is further discussed in §5.3.

3. Theoretical considerations

3.1. *Initial static shapes of the drops*

The orientation of the drops is shown in figure 1. The two drops are distorted differently, owing to their orientation with respect to gravity. The top pendent drop is stretched while the bottom sessile drop becomes flatter. The extent of this deformation is characterized by the capillary length for a particular liquid

$$a = \left(\frac{\sigma}{\rho g} \right)^{1/2},$$

where σ is the surface tension coefficient, ρ is the liquid density and g is gravity. For drop radius $R_d > a$, gravity will cause significant deviations from spherical form.

For precise characterization of the initial static drop shapes, we have numerically solved the differential equations describing these shapes, using the method described by Fordham (1948). The static drop shape represents a balance between hydrostatic pressure $\rho g z$ and the capillary pressure,

$$p_{cap} = p_{in} - p_{out} = \sigma \left(\frac{1}{R_1} + \frac{1}{R_2} \right), \tag{3.1}$$

where R_1 and R_2 are the principal radii of curvature of the free surface. The pressure inside the liquid at the bottom tip of the drop is determined solely by the tip radius of curvature, as $z = 0$ and $R_1 = R_2$, i.e. $p_{tip} = 2\sigma/R_t$. Here, we name these tip radii

of curvature R_t for the top drop and R_b for the bottom drop. Working in terms of gauge pressure, we set $p_{out} = 0$ and noting that the hydrostatic pressure decreases with height inside the top drop, the above balance states

$$\frac{1}{R_1} + \frac{1}{R_2} = \frac{2}{R_t} - \frac{\rho g z}{\sigma}.$$

We now normalize all lengths by the tip radius of curvature R_t or R_b and identify non-dimensional quantities with a star. In the cylindrical coordinates of figure 2(b) at each point (r^*, z^*) along the drop surface, we therefore have:

$$\kappa^* + \frac{\sin(\phi)}{r^*} = 2 + \beta z^*$$

where $1/\kappa^*$ is the radius of curvature at point (r^*, z^*) along the free surface, calculated in the z^*-direction and ϕ is the slope of the free surface, as shown in figure 2(b). $\beta = -\rho g R_t^2/\sigma$ is the Bond number. The sign of β changes between a pendent and a sessile drop.

These equations are now expressed in terms of arclength s along the free surface. The unknowns thus become $z^*(s)$, $r^*(s)$ and $\phi(s)$, as $\kappa^* = \mathrm{d}\phi/\mathrm{d}s$. The resulting set of three equations:

$$\frac{\mathrm{d}r^*}{\mathrm{d}s} = \cos\phi, \quad \frac{\mathrm{d}z^*}{\mathrm{d}s} = \sin\phi, \quad \frac{\mathrm{d}\phi}{\mathrm{d}s} = 2 + \beta z^* - \frac{\sin\phi}{r^*}, \tag{3.2}$$

are solved numerically, by a shooting method, based on guessing values for R_t and minimizing the least-squares difference between the calculated drop shape and the initial static drop shape obtained from the experimental image.

Figure 3(a) shows typical static drop shapes, compared to the inscribed circular shapes using the radii of curvatures at the contact point. Figure 3(b) shows the range of drop sizes tested herein. For the largest drop radii shown, we could only look at the very first contact as the liquid masses were not formed into drops, just two concave surfaces protruding slightly out of the nozzles. Boundary effects are in this case bound to be severe.

3.2. Dynamic model of the coalescence speed

Surface tension drives the motion and either inertia or viscous forces resist. The problem has no external velocity scale, as it starts from rest. Dimensional analysis supplies two such velocity scales, i.e. a capillary velocity, by balancing the capillary force with inertia

$$v_\sigma = \sqrt{\frac{\sigma}{\rho R_d}} \tag{3.3}$$

and the viscous velocity, by balancing viscous forces and surface tension, i.e. by setting the capillary number $Ca = \mu U/\sigma = 1$, where μ is the dynamic viscosity, which gives

$$v_\mu = \frac{\sigma}{\mu}. \tag{3.4}$$

We can form two separate Reynolds numbers based on these velocities,

$$Re_\sigma = \frac{\sqrt{\rho R_d \sigma}}{\mu} \tag{3.5}$$

using the capillary velocity and

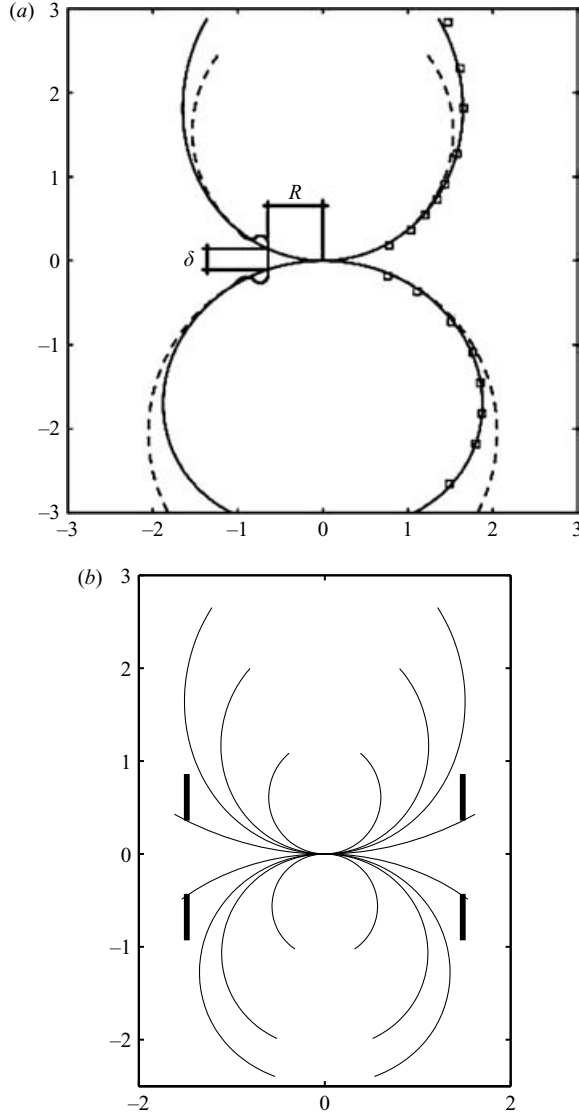$$Re_v = \frac{\rho R_d \sigma}{\mu^2} \tag{3.6}$$

FIGURE 3. (*a*) Static drop shapes compared to spherical drops. Broken lines are circles of the same radii as the radii of curvature at the contact point, $R_t = 1.53$ and $R_b = 2.05$ mm. The symbols show the measured shapes of the drops and the solid lines the static equilibrium shapes calculated by solving the differential equations. (*b*) Typical static drop shapes used herein, showing the range of drop sizes. The thick vertical line segments indicate the nozzle locations for the largest radii of curvature used herein. The axis units are in mm.

based on the viscous velocity scale above. The latter is simply the square of the first one. For the water drops, Re_v takes values in the range 0.35×10^5 to 1.0×10^5. For the most viscous glycerin/water solution used herein, this value becomes as small as 4×10^{-1}.

Herein, we use a model to predict the outwards motion of the radius of the contact region R, for low-viscosity liquids. It is based on balancing the capillary driving-pressure and the dynamic pressure of the fluid, ρu^2. Here, the driving pressure is

approximated as

$$\sigma\left(\frac{1}{\delta} - \frac{1}{R}\right),$$

where we have included both of the principal radii of curvature to get the 'total' capillary pressure. For this geometry, the two curvatures are of opposite sign, pulling the surface in opposite directions. Keep in mind that the capillary pressure in the liquid at the edge of the coalescence region is negative.

This gives us a model for the local outwards velocity of the neck region

$$\frac{\mathrm{d}R}{\mathrm{d}t} = C\sqrt{\frac{\sigma}{\rho}\left(\frac{1}{\delta} - \frac{1}{R}\right)}, \tag{3.7}$$

where δ is the vertical spacing of the two drop surfaces, as a function of R. This spacing is obtained using the actual static shapes of the drops (see figure 3), following the calculations in § 3.1. C is a proportionality constant to be determined from the data. Using δ instead of $\delta/2$ in comparison with $1/R$ is justified by the bulb which develops at the end of the advancing interface. When integrating (3.7), we use the observed initial radius of contact for the initial conditions $R(t=0)$. We will consider this inviscid model to be successful if C is a universal constant, independent of drop size and the value of the surface tension.

Similar ideas were put forth by Oguz & Prosperetti (1989) and by Eggers *et al.* (1999), as is clear from their derivation preceeding equation (5.1) reproduced in our discussion section. Essentially, the same model has successfully described the contraction of a thin disk of air caught under an impacting drop by Thoroddsen *et al.* (2003).

Here, we have assumed that gravity need only be included as far as it deforms the static drop shapes, but does not play a significant role in the coalescence dynamics. This becomes clear by considering the free-fall of a drop from rest. In the 2 ms duration of the coalescence of water drops, this drop would fall

$$h = \tfrac{1}{2}gt^2 = 20\,\mu\mathrm{m},$$

while the neck region grows to about 100 times that distance.

3.3. *Model in the viscous-dominated regime*

On purely dimensional grounds, the balance between surface tension and viscosity would predict a constant coalescence velocity as in equation (3.4). However, the asymptotic viscous theory of Eggers *et al.* (1999) has shown that the normalized neck radius $r_m^* = R/R_d$ grows as

$$r_m^*(t^*) \approx -\frac{1}{\pi}t^*\ln(t^*),$$

where the dimensionless time t^* is measured in units of $\mu R_d/\sigma$ and lengths are normalized by the drop radius R_d. Therefore, the velocity is made dimensionless by σ/μ. In real units, this equation states

$$\frac{R(t)}{R_d} \approx -\frac{1}{\pi}\frac{\sigma t}{\mu R_d}\ln\left(\frac{\sigma t}{\mu R_d}\right), \tag{3.8}$$

showing that the actual radius of the drop R_d affects the speed through a logarithmic dependence. In the above paper, the validity of this asymptotic theory is suggested for $r_m^* < 0.03$ and $Re < 1$. In our experiments these conditions are never satisfied, as
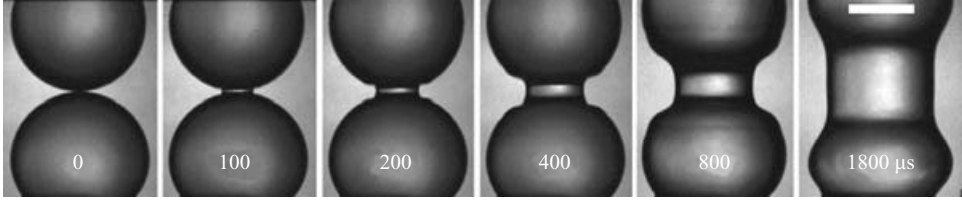
FIGURE 4. The surface shapes for coalescing water drops, $R_b = 1.15$ and $R_t = 1.08$ mm. Using needles with $D = 1.78$ mm and $H/D = 1.8$. Sequence taken with frame rate of 50 kHz. The scale bar is 1 mm long.
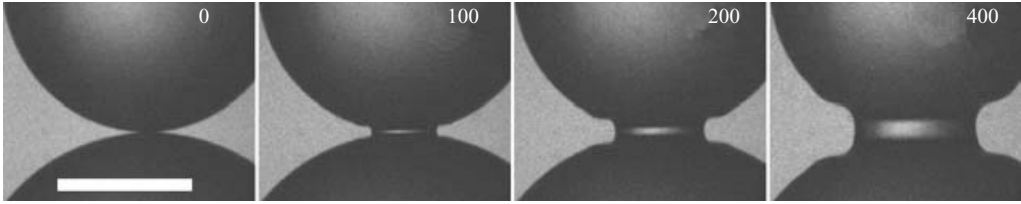

FIGURE 5. Close-up images of drop shapes during coalescence. From a different sequence to that in figure 4, taken at 200 kHz. $R_b = 1.36$ and $R_t = 1.04$ mm, using needles with $D = 1.78$ mm. The times are in μs and the scale bar is 1 mm long.

the initial R is about 60 μm which gives $r_m^* \sim 0.03$. Beyond this region of validity, the formula quickly diverges, only reaching a maximum neck radius of $r_m^* = 1/(\pi e) \simeq 0.12$.

Regarding the Reynolds number criterion, Eggers *et al.* (1999) point out that their viscous theory will always be valid, irrespective of the liquid viscosity, provided one goes to small enough diameters of the contact region. However, they also point out that for water drops, this viscous-dominated regime ends when the radius of the contact is about 10 nm, i.e. when the Reynolds number exceeds unity. The first contact observed herein for water drops is about 5000 times larger than this upper limit, thereby bypassing entirely the viscous-dominated regime, for water. For the most viscous glycerin/water mixtures this Re criteria is satisfied during the initial contact, as will be discussed in a later section.

4. Results

4.1. *Coalescence of water drops*

Figure 4 shows typical surface shapes during the coalescence of two water drops. Figure 5 shows a close-up of the phenomenon. The higher frame rate, used for the close-up images, requires larger gain for the sensing elements, making the images slightly grainy.

Image analysis on a sequence of individual video frames allows us to track the outwards motion of the neck region connecting the two drops. The time counter is, in what follows, set to zero at the last frame before first motion is observed. Figures 6 and 7 show this outwards motion and compare it to the model presented in the previous section.

The coefficient C is found from the best fit to the data by integrating relation (3.7), starting from the observed initial radius of the contact. Figure 6 shows excellent agreement with the model up to a radius of 70% of the average drop tip radii $R_{ave} = (R_t + R_b)/2$. We only use R_{ave} when the two radii are similar in size. For widely
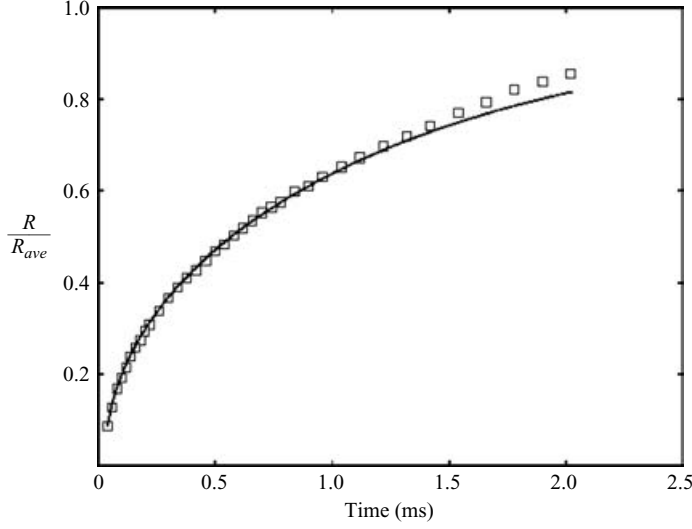
FIGURE 6. Coalescence speed, for the drop in figure 4. The solid curve
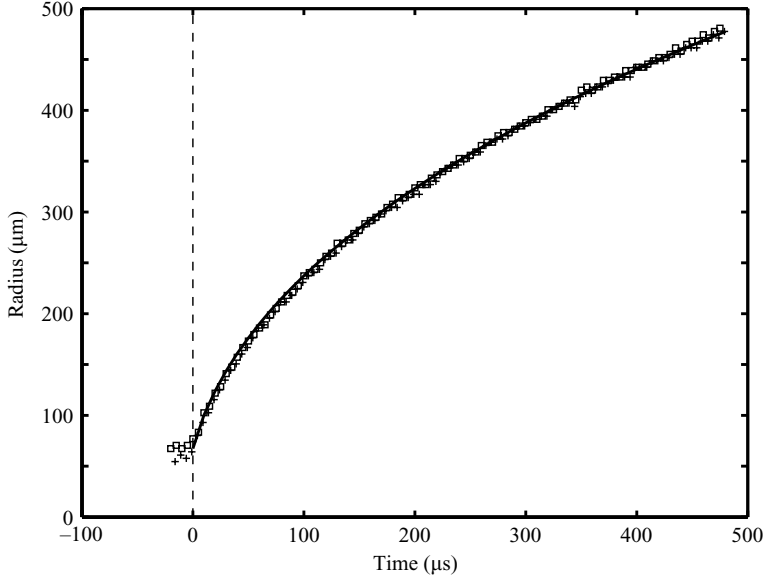shows the model fit with $C = 0.84$.

FIGURE 7. Early stage of coalescence, for two realizations ($\square$, $+$) one of which is shown in
figure 5. The other has drops with $R_b = 1.38$ and $R_t = 1.03$ mm. Radius in μm *vs.* time in μs.
First motion is observed about 20 μs after the electrical contact trigger. The solid line is the
predicted motion using equation (3.7) with $C = 0.80$. Ultra-high-speed camera frame rate was
200 kHz.

different radii or coalescence with a flat surface this definition is not appropriate. In
figure 7, for very early times, the curve showing the predicted values is indistinguishable
from the data, hiding behind the symbols.

Dozens of realizations were performed using different sets of needles to change the
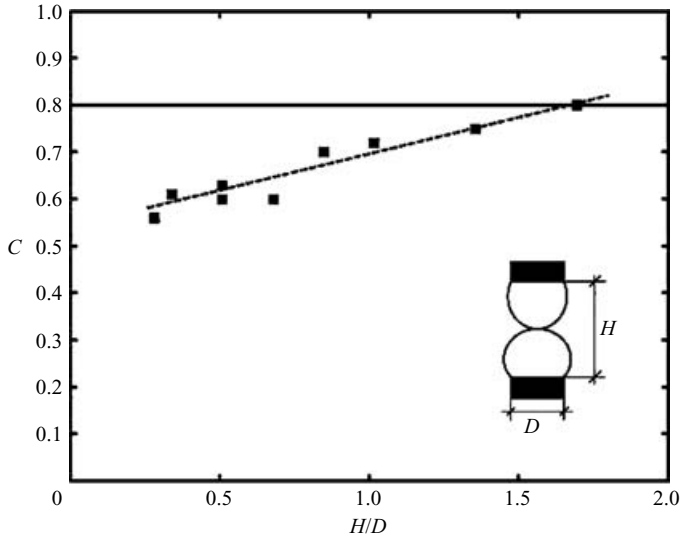drop diameters. It became clear that, for a given needle size, the vertical spacing H of

FIGURE 8. The best-fit coefficient C in (3.7) *vs.* the separation distance of the two needles. The needle diameters were both $D = 2.95\,\text{mm}$.

the two needles influences the value of the 'constant' C. By systematically varying this distance H, we constructed figure 8, which shows up to a 25% reduction in the value of C for very closely spaced needles, i.e. small value of H/D. The pinned boundaries of the drops clearly slow down the coalescence motions, when the boundaries are close to the neck region. By continuity, liquid has to move from the drops to fill in the growth of the neck region. This movement of drop liquid deforms the original drop surface. When the free surface is pinned close to the neck the original drop surface has to deform more to provide this liquid. Less surface energy is therefore released, slowing down the outwards motion of the neck.

   Large values of H/D will model the coalescence of free drops better. However, for large values of H, the drops become more deformed by gravity and the tip radii of curvature differ more. The bottom drop has a tendency to 'fall' off the needle and eventually the top drop will also pinch off. These practical considerations limit how large H can be set. It is, however, possible that even larger values of H/D could increase C somewhat, but we could not test this. This effect of small H/D might influence some of the results of Wu *et al.* (2004).

   Figure 9 shows that the value of C is independent of the size of the drops, keeping in mind the corrections for needle spacing which are applied for the largest and smallest drops (figure 12). These drops require close spacing of the needles as explained above. The constant value of C demonstrates the validity of the model in (3.7).

   The maximum outwards velocity occurs immediately following the first contact. From figure 7, we can estimate the initial velocity as $u_r = 2.9\,\text{m s}^{-1}$. For comparison, the very thin air disks caught under an impacting water drop (Thoroddsen *et al.* 2003) were observed to start contracting at speeds of the order of $10\,\text{m s}^{-1}$. Initial neck velocity of $3.6\,\text{m s}^{-1}$ was measured by Stover *et al.* (1997) for the coalescence of two bubbles of $375\,\mu\text{m}$ in diameter.

4.2. *Initial contact*

Figure 10 shows the earliest coalescence observed using the largest magnifications. Using a magnification of about 10, we can obtain an estimate of the initial diameter
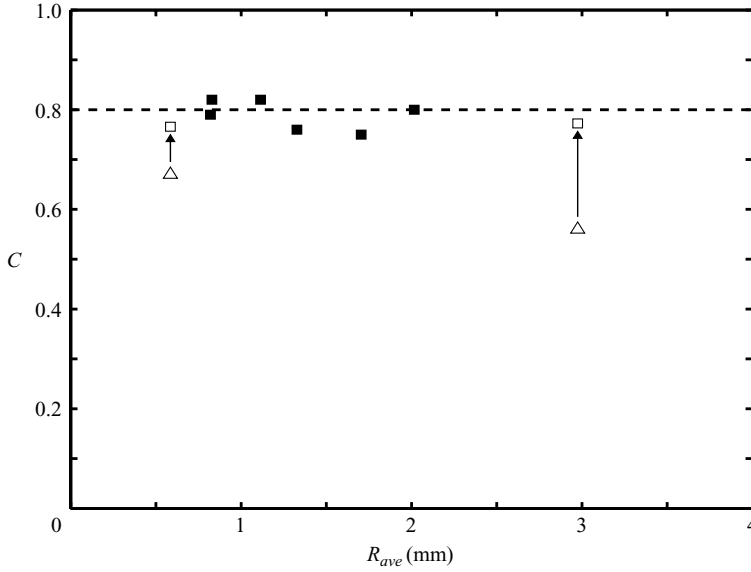
FIGURE 9. The best-fit coefficient C in (3.7) *vs.* the average radius of curvature of the drops. The first and last data points ($\triangle$) are corrected for the separation distance of the two needles ($\square$), according to the broken line in figure 8.
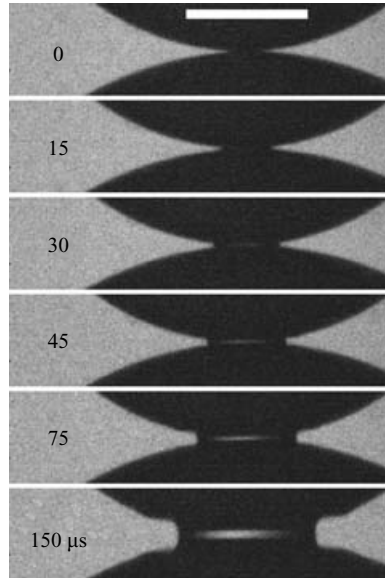

FIGURE 10. Earliest coalescence shapes for water drops. The scale bar is $500\,\mu\text{m}$ long.

of the contact region. From this video sequence, we obtain $128\,\mu\text{m}$ in diameter. For off-axis contact, this region can be even smaller. The diameter of the initial contact observed by Menchaca-Rocha *et al.* (2001) between mercury drops is $400\,\mu\text{m}$.

   This finite size of the initial contact also destroys any geometric self-similarity at the earliest times, so cherished by theoreticians. In the presence of air, the size of the initial region is bound to depend on the growth-rate of the drops before contact, or
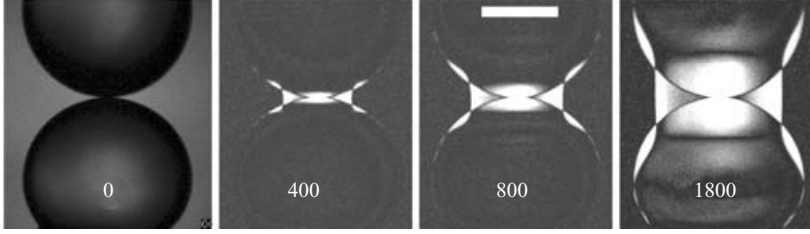
FIGURE 11. Evolution of the drop shapes during coalescence, from the same sequence as in figure 4. The three panels on the right show the absolute value of the intensity difference between the original image and the image of the evolved shape at the times indicated. The times are in µs and the scale bar is 1 mm long.
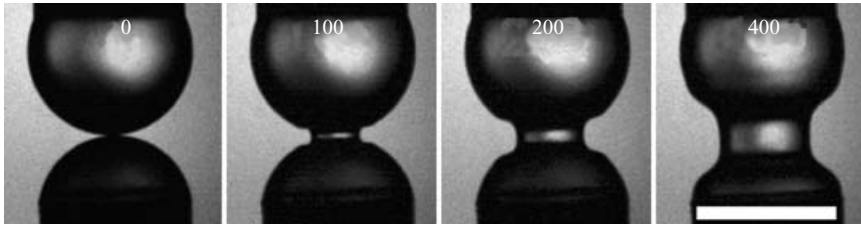

FIGURE 12. Evolution of the drop shapes during coalescence of the smallest drops tested, $R_b = 0.573$ and $R_t = 0.597$ mm. The value of C is here only 0.72, consistent with boundary effects due to the small value of $H/D = 1.2$. The times are in µs and the scale bar is 1 mm long.

in other words their speed of approach. The air being push out of the gap between the drops will introduce a pressure gradient, which will deform the contact region, making the drops flatter. This may lead to an outer contact along a ring, as discussed in § 5.3.

Figure 11 shows the relative changes in the surface shapes, by subtracting the original image. The difference panels show the absolute value of the pixel intensities. It is clear from these images that the deformation of the free surface is fairly local, with the original drop shapes unchanged far from the neck region. However, a small-amplitude capillary wave propagates along the drop surfaces. This wave has travelled about 90° from the contact point, after only 800 µs from first contact. As most of the free-surface deformation occurs close to the neck region, this allows us to measure directly from the video frames, how the total surface area reduces in time.

4.3. *Coalescence of alcohol drops*

A limited number of experiments were conducted using alcohol drops to reduce the surface tension. To enable the triggering, we used a mixture of 98% alcohol and 2% DI water. The capillary length for alcohol is 1.9 mm, which is significantly smaller than that for water, which is 2.8 mm. The drops are therefore more deformed by gravity. The results show an identical time-curve to those for water, as shown in figure 13. The best-fit coefficients are also very similar.

From the results for water and alcohol drops we conclude that the constant in relation (3.7) takes the value $C = 0.80 \pm 0.05$.
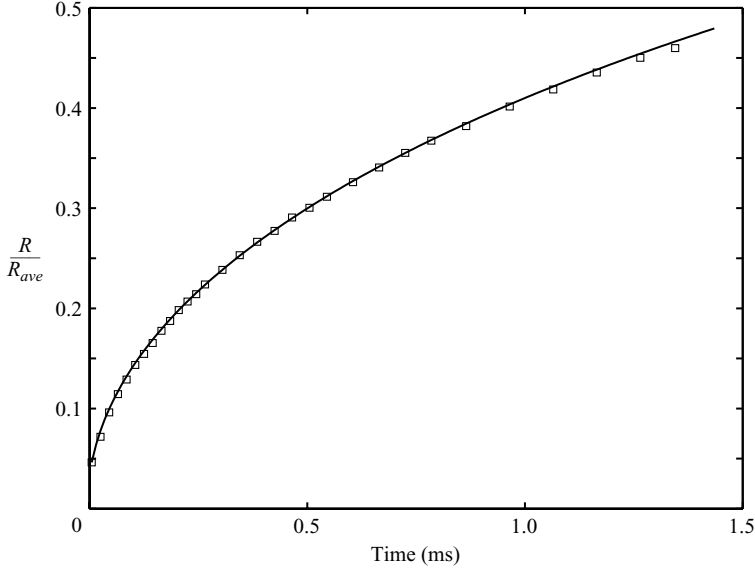
FIGURE 13. Coalescence motions for 98% alcohol drops ($\sigma = 0.027$, $\rho = 794 \, \mathrm{kg \, m^{-3}}$), using needles with $D = 2.95 \, \mathrm{mm}$, giving drops of $R_t = 1.28$, $R_b = 1.68 \, \mathrm{mm}$. Included is the best curve-fit with $C = 0.84$.
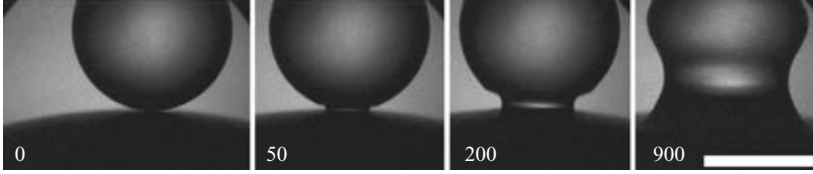

FIGURE 14. Coalescence of water drops of widely different radii. The needle diameters are $D_t = 1.09$ and $D_b = 8 \, \mathrm{mm}$, giving $R_t = 0.72$, $R_b = 6.6 \, \mathrm{mm}$. The scale bar is 1 mm long.

4.4. *Coalescence of drops having widely different radii*

Some experiments were performed using differently sized needles, i.e. with a top metallic needle of 1.09 mm while the bottom nozzle was a plastic gate-valve 8 mm in diameter, as shown in figure 14. This was compared with data using two needles of diameter 2.95 mm, which were taken in the same set of measurements. Figure 15 demonstrates that the best fit coefficient C has very similar values irrespective of the difference between the top and bottom radii of curvature. The values are slightly lower than 0.8, but no attempt was made to correct for any H/D effects here. This shows that vertical spacing of the liquid surfaces δ is the primary parameter of importance in the dynamics. The drop radii do, of course, determine the physical size of this spacing, but have been absorbed into δ.

   This invariance to the difference in top and bottom drop radii is discussed in §5.5, with respect to the well-known generation of a vortex ring when a drop coalesces with a flat liquid surface.

4.5. *Effects of increasing liquid viscosity*

Experiments were conducted with glycerin/water mixtures to investigate the slow-down of the coalescence due to viscous forces. Figures 16 shows the drop shapes during coalescence for the most viscous liquid used. The most striking difference in
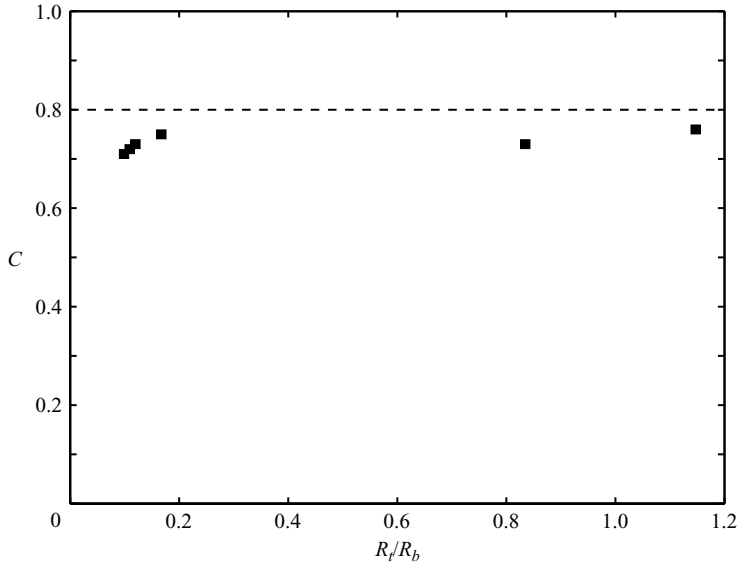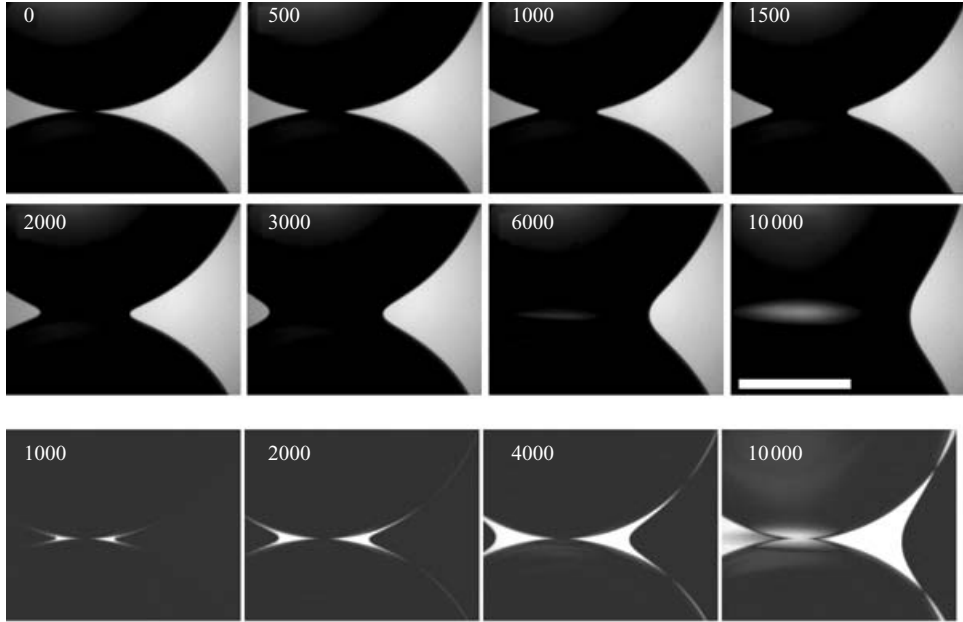
FIGURE 15. Coefficient C *vs.* the ratio of the drop sizes.

FIGURE 16. Coalescence shapes for the most viscous drops (96% glycerin, $\mu = 0.493\,\mathrm{Ns\,m^{-2}}$, $\sigma = 0.065$, $\rho = 1250\,\mathrm{kg\,m^{-3}}$), using needles with $D = 2.95\,\mathrm{mm}$, giving $R_t = 1.42$, $R_b = 1.55\,\mathrm{mm}$. The bottom row shows differences in the drop shapes between the static image and the corresponding shapes at the times indicated. Times are in µs and the scale bar is 1 mm long.

shape between the high- and low-viscosity liquids is the sharpness of the neck region, as can be expected from examining the two-dimensional shapes presented by Hopper (1992) for the viscous case and by Keller & Miksis (1983) for the inviscid case. This change in neck curvature will be quantified below. The bottom panels in figure 16
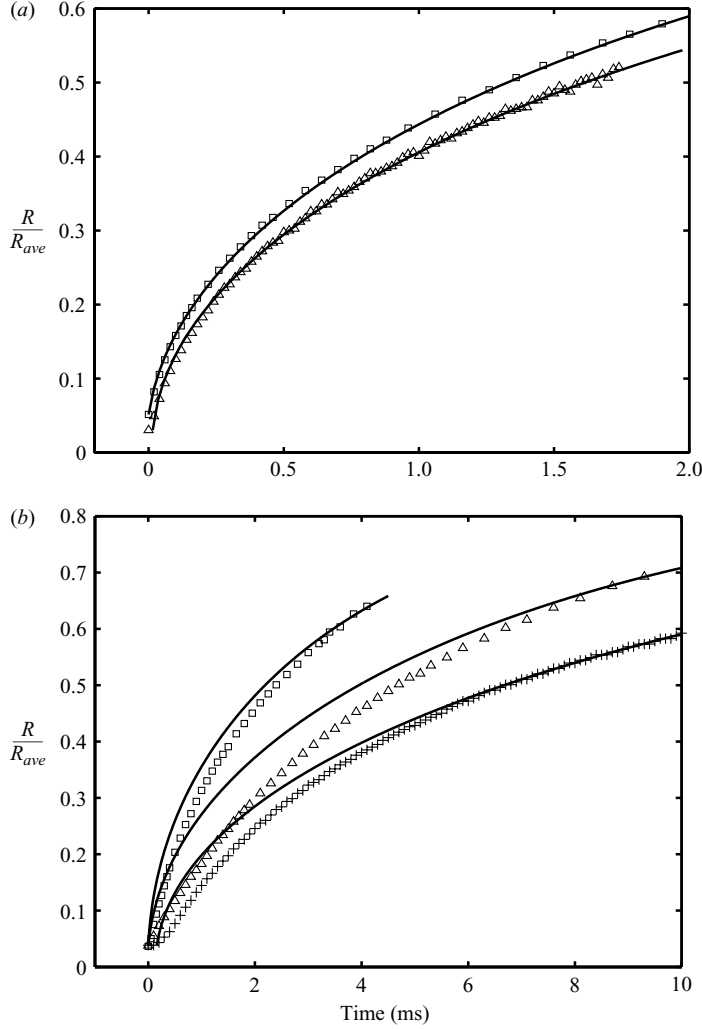
(*a*)

(*b*)

FIGURE 17. Coalescence for different concentrations of glycerin/water mixtures. (*a*) Low concentrations of glycerin. □, 25% glycerin ($\sigma = 0.070 \, \text{N m}^{-1}$, $\rho = 1062 \, \text{kg m}^{-3}$, $\mu = 2.2 \times 10^{-3} \, \text{Ns m}^{-2}$), $R_t = 1.50$, $R_b = 1.54 \, \text{mm}$. The best-fit coefficient $C = 0.75$. △, 50% glycerin ($\sigma = 0.068 \, \text{N m}^{-1}$, $\rho = 1130 \, \text{kg m}^{-3}$, $\mu = 7.2 \times 10^{-3} \, \text{Ns m}^{-2}$), $R_t = 1.43$, $R_b = 1.62 \, \text{mm}$. The best-fit coefficient $C = 0.64$. (*b*) High concentrations of glycerin. □, 75% glycerin ($\sigma = 0.066 \, \text{N m}^{-1}$, $\rho = 1188 \, \text{kg m}^{-3}$, $\mu = 43 \times 10^{-3} \, \text{Ns m}^{-2}$), $R_t = 1.36$, $R_b = 1.77 \, \text{mm}$. The best-fit coefficient $C = 0.52$. △, 90% glycerin ($\sigma = 0.065 \, \text{N m}^{-1}$, $\rho = 1225 \, \text{kg m}^{-3}$, $\mu = 0.220 \, \text{Ns m}^{-2}$), $R_t = 1.47$, $R_b = 1.53 \, \text{mm}$. The best-fit coefficient $C = 0.28$. +, 96% glycerin ($\sigma = 0.065 \, \text{N m}^{-1}$, $\rho = 1250 \, \text{kg m}^{-3}$, $\mu = 0.493 \, \text{Ns m}^{-2}$), $R_t = 1.42$, $R_b = 1.55 \, \text{mm}$. The best-fit coefficient $C = 0.16$. The radial coordinates are normalized by the average radii of curvature. The needle diameters were both $D = 2.95 \, \text{mm}$.

show the intensity differences from the original shapes. The deformation of the drop is more gradual and does not show capillary waves.

Figure 17 shows the effect of increasing the viscosity on the coalescence speed of the drops. Figure 17(*a*) shows the speed for the weaker concentrations of glycerin used, i.e. 25% and 50%. Viscosity has already started to slow down the coalescence for 50% glycerin. The coefficient *C* has reduced by about 15% while the shape of
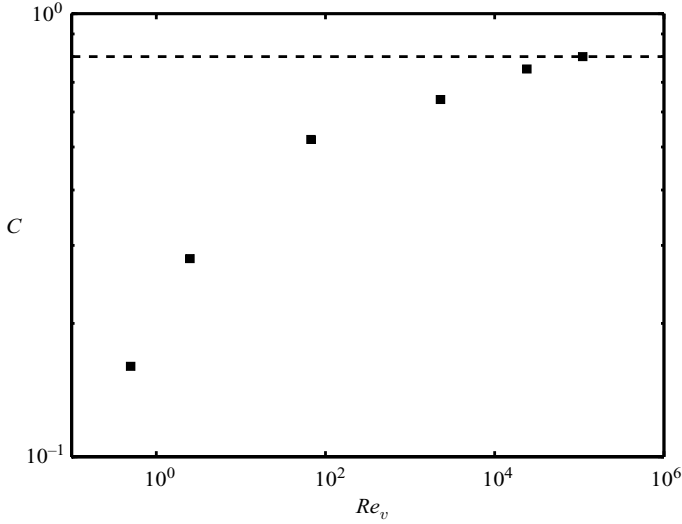
FIGURE 18. The best-fit coefficient C in (3.7) *vs.* drop $Re_v = \rho R_{ave}\sigma/\mu^2$. The broken line is the low viscosity value $C = 0.80$ determined using water drops.

the curve is not affected. Further increase in viscosity not only slows the coalescence further, but changes qualitatively the shape of the curve, as shown in figure 17(*b*). The values of C for these higher viscosities show a clear trend, but are quite subjective, depending on where along the curve we choose to match the line with the data. Figure 18 shows the reduction in C with increasing viscosity, i.e. with reduction in the Reynolds number.

For the largest viscosity (figure 16), the free surface far away from the neck is significantly disturbed early on. The image differences show movement at the outer edge of the image, at about $4000\,\mu$s after first contact. We can therefore only measure reliably the release of surface area up to that point in time, as our images are zoomed in on the neck region.

Figure 19 shows that, for the largest viscosity, the speed is approximately constant during the first $2500\,\mu$s. The linear fit to this region shows a outwards velocity of $u_r = 0.16\,\mathrm{m\,s^{-1}}$. Note that some of the realizations show a slightly lower initial velocity before this linear region. This may be due to the finite initial contact radius. The Reynolds number based on the instantaneous neck-radius r, as in Eggers *et al.* (1999)

$$Re_{v*} = \frac{\rho r \sigma}{\mu^2}, \tag{4.1}$$

is here at first contact ~ 0.02 and grows to $Re_{v*} \simeq 0.12$ where the data start to deviate from this linear region, corresponding to $R \simeq 0.22 R_{ave}$.

If we assume that the capillary viscous balance governs the motions in this region, we would expect a velocity of approximately $u_r \simeq \sigma/\mu = 0.13\,\mathrm{m\,s^{-1}}$ which is surprisingly close to the observed value. The formula (3.8) taken from Eggers *et al.* (1999) predicts a radial velocity of $u_r \simeq -\sigma[1 + \ln(\sigma t/\mu R)]/(\pi\mu)$, which in contrast with the measurements, is monotonically decreasing with radius and time. For the fluid properties in figure 19, the equation predicts $u_r = 0.115\,\mathrm{m\,s^{-1}}$ at $R/R_{ave} = 0.03$ and reduces to $u_r = 0.07\,\mathrm{m\,s^{-1}}$ at $R/R_{ave} = 0.06$. The latter radius is outside the intended region of applicability of this theory, but the former velocity is of the same order of magnitude as the measurements.
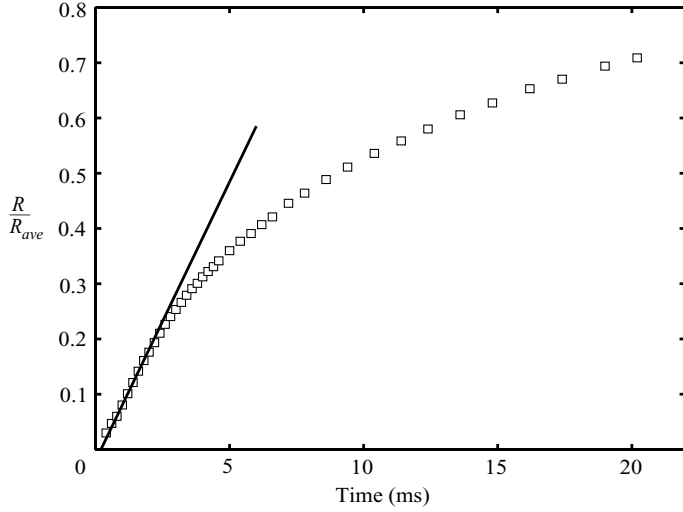
FIGURE 19. Coalescence speed for 96% glycerin/water drops ($\sigma = 0.065\,\mathrm{N\,m^{-1}}$, $\rho = 1250\,\mathrm{kg\,m^{-3}}$, $\mu = 0.493\,\mathrm{Ns\,m^{-2}}$). Using needles with $D = 2.95\,\mathrm{mm}$, giving $R_t = 1.45$, $R_b = 1.88\,\mathrm{mm}$. The line shows a velocity of $0.16\,\mathrm{m\,s^{-1}}$.
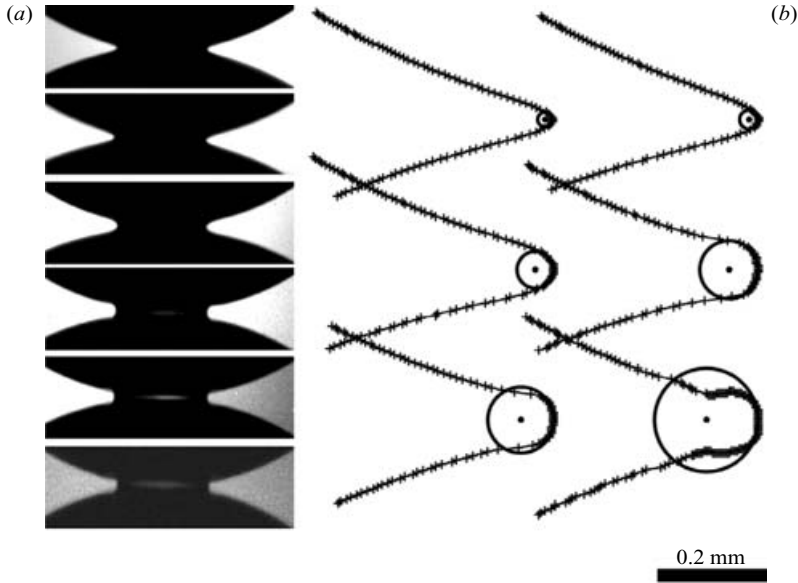

FIGURE 20. Neck shapes for different viscosities. The neck diameters are $560\,\mu\mathrm{m}$. The viscosity increases from the bottom image up and has values of $(1.00, 2.17, 7.15, 42.6, 220$ and $493)$ $\times 10^{-3}\,\mathrm{Ns\,m^{-2}}$, respectively.

4.6. *Neck curvature vs. viscosity*

Figure 20(a) shows close-up images of the shape changes in the neck region when viscosity is increased. Here, we have chosen to fix the neck diameter for all the cases. The video frames allow us to estimate the vertical curvature in the neck region. We have done this by fitting inscribed circles to the surface shape. This was done interactively and therefore contains some subjectivity, such as to how many data
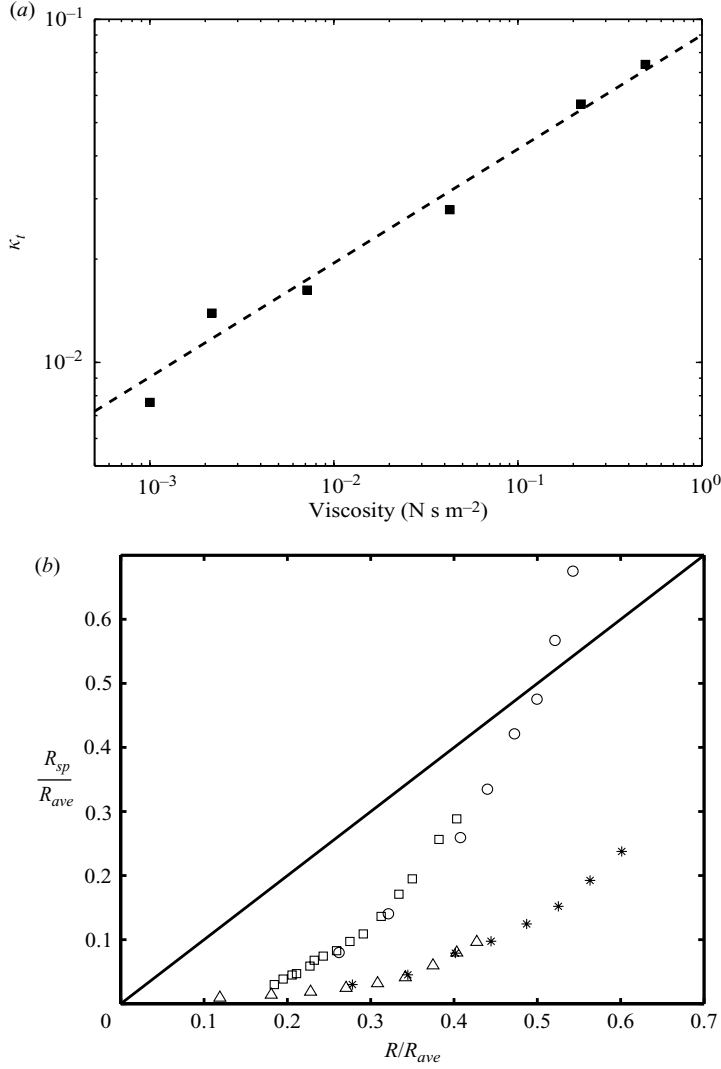
FIGURE 21. The curvature of the free surface in the neck region. (*a*) Total curvature (equation (4.2)) measured from figure 20, *vs*. liquid viscosity. The broken line has a slope of $1/3$. (*b*) The radius of the inscribed circle R_{sp} *vs*. the neck radius R, for pure water ($\square$, $\bigcirc$) and 96% glycerin ($\triangle$, $*$).

points are used to find the 'best-fit' circles. Figure 21 shows how the total curvature

$$\kappa_t = \left(\frac{1}{R_{sp}} - \frac{1}{R} \right) \tag{4.2}$$

changes as a function of viscosity. Here, R_{sp} is the radius of the inscribed circles in figure 20(*b*). This radius varies from 12.9 to 89 μm for the 6 different viscosities shown in the figure, whereas the neck radius is fixed at $R = 280$ μm for all. The neck becomes progressively sharper as the viscosity increases. With lower viscosity, a capillary wave crest appears to precede the neck region, very similar to the results of Keller *et al.* (2000). The broken line in figure 21(*a*) has a slope of $1/3$ and is just intended to guide the eye.

Figure 21(b) shows the change in the radius of curvature R_{sp} during the coalescence, as the neck radius R grows. Results are shown for the largest and smallest viscosities. R_{sp} was again estimated by manually fitting inscribed circles to the images. This could not be done accurately for the smallest values of R, owing to the limited pixel resolution. The results show that the much sharper relative curvature for the viscous dominated motions, persists during all of the coalescence. While for the inertia dominated regime, the vertical curvature reduces rapidly during the coalescence, with the total curvature even falling to zero, i.e. where the data points cross over the line $R_{sp} = R$, with the surface tension now slowing the intertial motions. Keep in mind that the inscribed circle tries to estimate the curvature only around the centreline, where the curvature was even observed to change sign in Keller *et al.* (2003).

5. Discussion

In this section, we will expand on the description of the results and compare them to previous studies.

The only previous measurements of the initial coalescence motions were accomplished by Menchaca-Rocha *et al.* (2001). Most of their measurements are focused on times larger than 1 ms after first contact. However, a few of their measurements were taken at 50 kHz starting at times as early as 10 µs after first electrical contact, giving comparable temporal resolution to that obtained here. These remarkable measurements were conducted with an 8-frame 'analog camera'. As mentioned earlier, their set-up is significantly different from ours. They used sessile mercury drops sitting on a glass plate. In this way, they succeed in producing nearly identical drops free of the differential distortions of our two drops, owing to their orientation w.r.t. gravity. However, by using two sessile drops, one sacrifices axisymmetry about the axis connecting the two drop centres, as gravity makes the vertical and horizontal curvatures different. This becomes progressively more pronounced as the drops are made larger. The curvature in the vertical plane is larger than that in the horizontal plane, whereas the separation of the free surfaces δ changes more slowly in the horizontal direction, therefore driving the overall coalescence motions. This difference in the two principal radii of curvature also raises the possibility of shape oscillations in the neck cross-sections. Despite the large surface tension of mercury, its very large density makes mercury drops less spherical than water drops. The capillary length for mercury is 1.9 mm compared to that for water which is 2.8 mm. Their configuration is, on the other hand, free of the boundary effects due to the pinning at our needles. For all these reasons, we do not expect perfect agreement with the present results, in what follows.

Comparison with direct numerical simulations is difficult, as even the most sophisticated numerical methods seem to have problems with the very earliest motions, as is evident in the numerical section of Menchaca-Rocha *et al.* (2001). Wu *et al.* (2004) also find poor comparison with the coalescence speed from the inviscid results of Duchemin, Eggers & Josserand (2003). This can be expected, as Duchemin *et al.* (2003) focus on the very early stage of the coalescence where they find repeated reconnections and entrapment of toroidal 'bubbles' or 'voids'. The experiments appear to bypass this intial stage, owing to finite intial contact radius caused by the lubrication pressure in the air.

5.1. *Power-law scaling*

Because of recent interest in self-similar universal solutions for free-surface flows and their 'singularities', many studies have focused on the appearance of power-law scaling for some physical quantities, e.g. Eggers (1997) and Zeff *et al.* (2000).

Eggers *et al.* (1999) concentrate on viscous-dominated coalescence, but also include a dimensional argument for the inviscid case, where they predict that the radial growth of the neck has a power-law dependence on time. They assume that the interfacial stress driving this motion is $\sigma R_d/r^2$, where R_d and r are the drop radius and the neck radius, respectively. This stress should be balanced by the dynamic pressure ρv^2. By setting $v = \mathrm{d}r/\mathrm{d}t$ they obtain a differential equation for the radius, i.e.

$$\left(\frac{\mathrm{d}r_m}{\mathrm{d}t}\right)^2 \propto \frac{\sigma R_d}{\rho r_m^2} \Rightarrow \frac{\mathrm{d}r_m}{\mathrm{d}t} \propto \left(\frac{\sigma R_d}{\rho}\right)^{1/2} \frac{1}{r_m},$$

which has the solution

$$r_m \propto \left(\frac{\sigma R_d}{\rho}\right)^{1/4} t^{1/2}. \tag{5.1}$$

These authors expect this power law to be valid only for $r \ll R_d$. They use $r/R_d < 0.03$ as a rule of thumb in their viscous theory. Here we take the liberty of comparing our data to their inviscid theory up to much larger radii. Duchemin *et al.* (2003) describe in more detail the subtleties involved in the above balance.

Menchaca-Rocha *et al.* (2001) applied such a power-law scaling to their data, i.e. $r \propto t^\alpha$, obtaining values for α of 0.41 for large radii and 0.55 for the earliest times. These values are in reasonable agreement with the above prediction of $\alpha = 0.5$.

For completeness, we have also compared our results with these power laws. We have chosen drops where $H/D > 1.5$ and the bottom radii R_t and R_b are similar. Figure 22(a) shows the data compared to the predicted exponent of 1/2. The data deviate clearly from this power law at the largest neck radii. This is not unexpected, as the arguments underlying this prediction were only intended to apply for very small R/R_{ave}. This fall-off in α is very similar to that observed by Menchaca-Rocha *et al.* (2001). The best-fit line, through the last 16 data points, in figure 22(a), i.e. for the largest R/R_{ave} values, gives a slope of 0.408, This is identical to the slope mentioned above for sessile mercury drops. This may be surprising, considering the widely different boundary conditions in the two studies.

Power laws require a known origin for the time, which is not easily observed from the experiments. The data-points for the earliest times in figure 22(a), suffer large uncertainties in the determination of t_o, owing to the relatively slow sample rate, which was 50 kHz for this realization. Figure 22(b) shows a similar log–log plot for a sequence sampled at 200 kHz, which identifies the origin of time with more certainty. Here, the power law is also weaker than 0.5, with a best-fit slope of 0.46. Menchaca-Rocha *et al.* (2001) report a steeper slope of 0.55 from their earliest data-points. However, this value is highly dependent on the choice of origin for their time-axis. This is demonstrated in figure 23, where we have looked at their data and shifted the zero time by subtracting 25 and 50 μs. We have also left out the first data points from the exponential fits. The figure shows that this shifting can produce slopes both larger and smaller than 0.5. It is therefore quite critical to determine whether the electrical contact and the fluid contact occur exactly simultaneously. This is a question which we cannot answer with certainty, neither for their data nor for ours. However, the strong dependence of the exponent on slight variations in t_o is clear.

The slight deviation of the observed slopes from 0.50 may be due to the finite initial radius of the contact, i.e. because the drops do not meet at a point as the theory presumes. In other words, the capillary pressure must initially accelerate more liquid than if the contact were at a point and the neck motions were given a flying start. The effects of a finite initial contact radius is aggravated by the observation that the release of surface energy is fastest at first contact, as will be shown in the
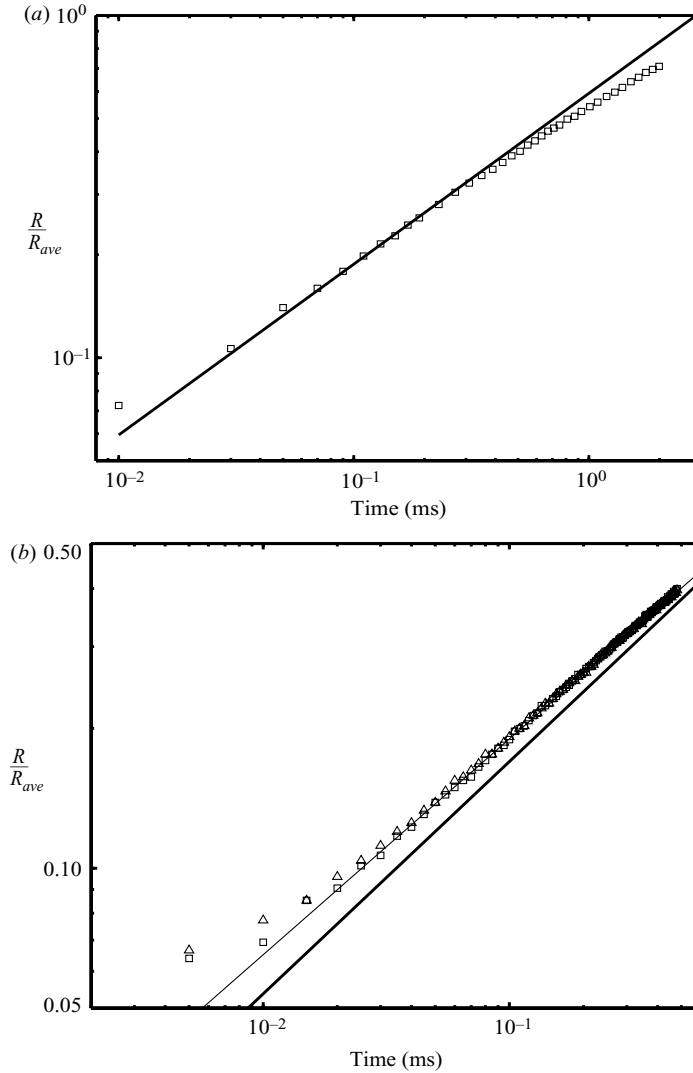
FIGURE 22. The coalescence motions on a log–log plot. (*a*) Data from figure 6. The line has a slope of 0.50. Data taken using frame rate of 50 kHz. (*b*) The coalescence shown in figure 7 on a log–log plot. The bold line has a slope of 0.50, whereas the best-fit thin line has a slope of 0.46.

following subsection. Experiments in a vacuum would be valuable to address this issue, as the contact should occur closer to a point, resulting in much larger initial outwards velocities and a larger range over which to test the power law. The reduced angle of the contact might also lead to entrapment of bubble rings, as proposed by Duchemin *et al.* (2003), Keller *et al.* (2003) and Oguz & Prosperetti (1989).

The effects of viscous forces on these power laws were investigated by looking at the water/glycerin solutions. Figure 24 shows that none of the data show a clear power-law scaling over the whole time-span, while there is a general trend with the slopes increasing with larger viscosities. A constant velocity, as was observed in part of figure 19, would give a slope of 1.
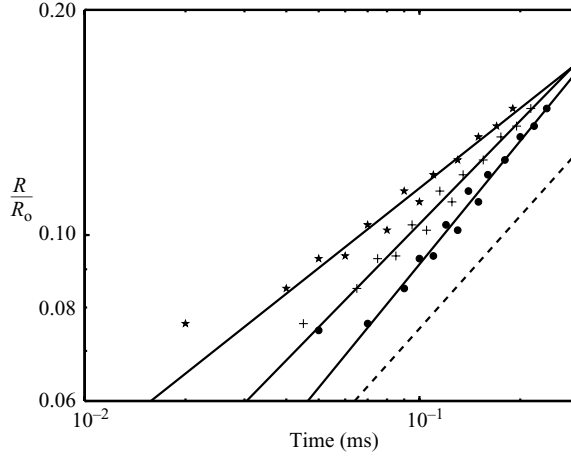
FIGURE 23. The effect of shifting the origin of the time axis on the exponent in the power law. ●, the original data from Menchaca-Roca *et al.* (2001), with the best-fit exponential of 0.55. +, data when the origin has been shifted by subtracting 25 μs. The best-fit exponential is now 0.46. *, time is now shifted by 50 μs, giving an exponent of 0.35. The broken line has a slope of 0.5.

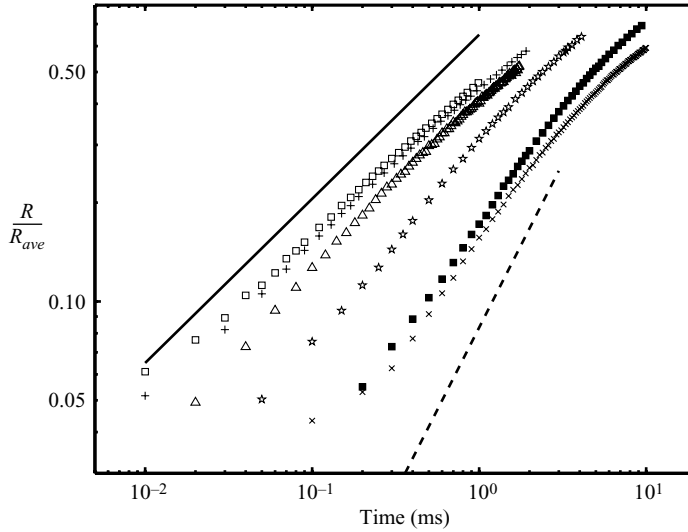FIGURE 24. The effect of viscosity on the power-law scaling of the radial motions. From left to right the (□, +, △, ⋆, ■, ×)-symbols correspond to viscosities of (1.00, 2.17, 7.15, 42.6, 220 and 493) × 10^{-3} Ns m^{-2} respectively. The solid line has a slope of 0.5 and the dashed line a slope of 1.0.

The power-law dependence on the liquid properties is different in (5.1) from Eggers *et al.* (1999) and, in the equation, we propose (3.7). Comparing data for different liquids, such as alcohol, water and mercury, this dependence can be investigated. Unfortunately, the range of liquid properties is not sufficiently large to distinguish between the different models.

5.2. *Release of surface energy*

The coalescence motions are driven by the release of surface energy $\sigma \, \Delta S$. For the idealized case of two spherical drops of radii R_1 and R_2 which coalesce to form a new drop R_3, volume conservation dictates that

$$R_3 = \left(R_1^3 + R_2^3\right)^{1/3},$$

with the corresponding reduction in surface area S

$$\Delta S = S_3 - (S_1 + S_2) = 4\pi\left[\left(R_1^3 + R_2^3\right)^{2/3} - \left(R_1^2 + R_2^2\right)\right].$$

If $R_1 = R_2$, the fraction of surface energy released becomes

$$\frac{-\Delta S}{S_1 + S_2} = 1 - 2^{-1/3} = 0.206, \tag{5.2}$$

which shows that rather a small fraction of the initial surface energy is released during the coalescence. For reference, consider two water drops with $R_1 = R_2 = 1$ mm. If all of the released energy were converted, without losses, into translational kinetic energy of the combined drop, its velocity would become $0.3 \, \mathrm{m \, s^{-1}}$. This shows clearly that only a small fraction of the drop liquid participates in the rapid coalescence motions, which are as much as 10 times faster (see figure 7), therefore giving some fluid elements 100 times that average kinetic energy.

Our drops are pinned at the needles and therefore have less free-surface energy to release. However, for large separation of the needles, this will not affect the initial motions, which are concentrated in the neck region.

The area of the free surface was integrated from the video images, using the axisymmetry. Image processing using edge-detection identified the pixels on the drop edges, as shown in figure 25(a). Polynomial fits to the 'jagged' pixel data were used to calculate the area. This had to be done in segments, owing to the sharp curvature in the neck region.

Figure 25(b) shows the release of surface energy during both the coalescence of water drops and of 96% glycerin drops. The areas have been normalized by the area of spheres having the radii of the tip radii of curvatures of the static drops, i.e. $S_o = 4\pi(R_t^2 + R_b^2)$. The coalescence for the two different viscosities show significant qualitative differences in the energy release. The inviscid case shows maximum rate of release at first contact, with a monotonically decreasing rate, whereas the viscous case shows a constant rate of decrease in surface area from 0.5 to 3 ms after first contact, with the short initial period of slower release of energy. This is consistent with the slightly lower initial velocities which are observed for some of the most viscous realizations, see figure 19.

5.3. *The radius of initial contact*

The original neck sizes observed herein are about $120 \, \mu\mathrm{m}$ in diameter. Assuming the contact is along a ring, this should trap an air-disk of approximately $100 \, \mu\mathrm{m}$ in diameter. For drops of 0.8 mm in radius, this represents only 0.4% of their original area and is therefore rather insignificant in the overall dynamics, even though this represents 2% of the total released area in (5.2). However, this energy is released very quickly and the very first motions might be affected by the contraction of this air-disk into one or two bubbles at the centreline, see Thoroddsen *et al.* (2003) and photographs by Peck & Sigurdson (1994). The contraction of this air-disk will induce
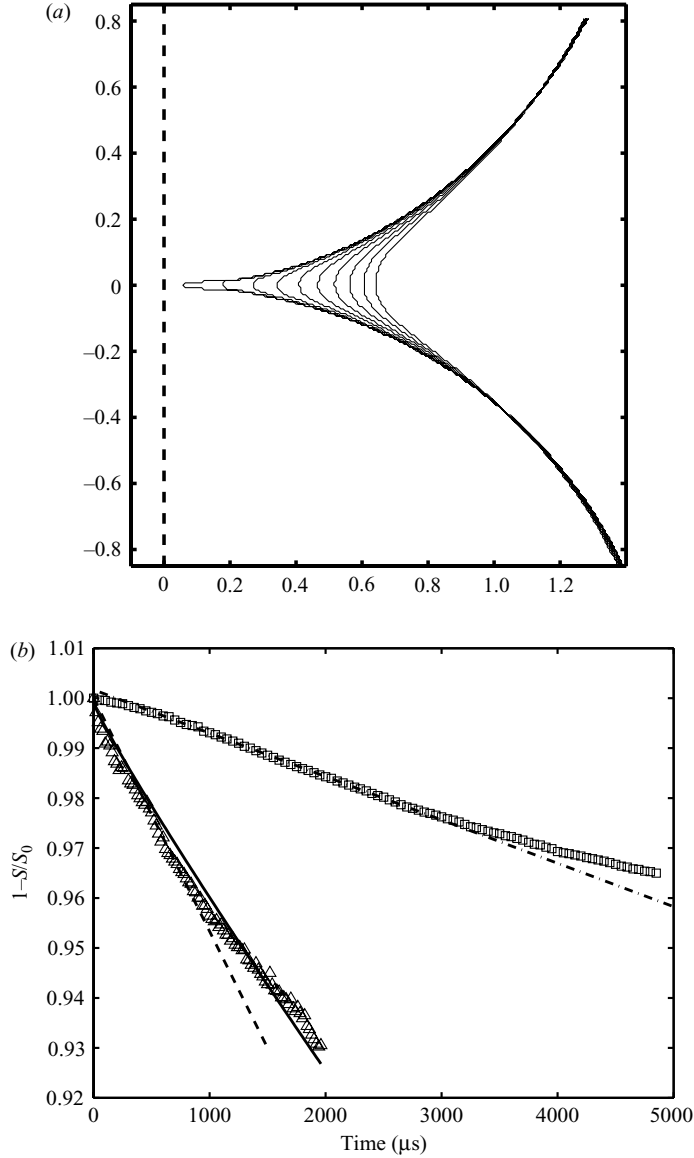
FIGURE 25. (*a*) Coalescence shapes for 96% glycerin, $\mu = 0.493 \, \text{Ns m}^{-2}$. The surface profiles are separated by 500 µs, starting from first contact. The broken line marks the drop centrelines. The axes are in units of mm. (*b*) The release of surface area during drop coalescence. The areas have been normalized as explained in the text. □, large viscosity, 96 % glycerin; △, water.

velocities in the opposite direction to the overall outwards motions driven by the outer edge. This may therefore slow down the motion during the first few micro-seconds after first contact. If the thickness of the entrapped air sheet were known, this effect could be estimated, but the present optical set-up is not up to this task. Without measuring precisely the approach velocity of the drops, we can neither calculate this thickness, nor find the force pushing the two drops together. We can however, find a rough estimate of the dimple radius b over which the drops are deformed, by taking the balance between the surface tension and the weight pushing the surfaces together,

see Rother *et al.* (1997). This suggests $\pi b^2 \sigma / R_d \simeq \Delta \rho g R_d^3$, which gives us

$$b \simeq \sqrt{\Delta \rho\, g / (\pi \sigma)}\; R_d^2. \tag{5.3}$$

Rother *et al.* (1997) represent R_d by the reduced radius $R_1 R_2 / (R_1 + R_2)$ which gives the normalized radius of the disk as $r/b \simeq 1$. For our typical water drops of $R_t = R_b = 1$ mm, the reduced radius becomes $R_d = 0.5$ mm and this equation gives $b = 50\,\mu$m, consistent with the smallest initial contact radii, observed in the experiments, of about $60\,\mu$m. This close agreement is probably coincidental, but indicates that the observed initial radius represents a physically reasonable value. The electrical trigger might also affect the size of the initial contact, by electrostatic forces which might pull the two surfaces together. As discussed earlier, the trigger circuit was designed to minimize the electrical current following the contact, so that even if electric forces affect the size of the initial contact, we do not expect them to influence the subsequent dynamics of the coalescence. Triggering based on a different principle, possibly using the blockage of a laser beam by the advancing contact, would eliminate such electrical effects. We can also consider the possibility that the contact might occur at a point and the initial motions might not be observed owing to slight misalignments of the optical axis from the horizontal. Point contact might be promoted by the static charge due to the trigger, counteracting the formation of a dimple by the lubrication pressure. This is consistent with the data in figure 7, where we can extrapolate the solid curve down to zero radius and find that it intersects the time axis approximately at the time of the electrical trigger, i.e. $20\,\mu$s before the first observed motion. The fact we do not notice a bubble inside the contact region, is also consistent with a point contact. However, the entrapped bubble would probably be quite small and could be hidden by light refraction from the highly curved free surface. We should mention that shifting the time-axis in figure 22(*b*) destroys the power law, making the data points for the first $100\,\mu$s lie close to a slope of 0.63, see the discussion on figure 23. We conclude that the two scenarios, of the contact at a point and along a ring, seem compatible with the data, and measurements using different optical set-ups are required to determine conclusively which occurs.

5.4. *Intermediate viscosities*

The theories mentioned above deal either with the inviscid or the viscous-dominated regimes. A theory of coalescence at intermediate Reynolds numbers is not available for comparison. We have, however, noticed by trial and error, that the data in figure 17(*b*) fall close to the same curve if we divide the time-axis by $\sqrt{\mu}$, as is shown in figure 26. We have, however, no theory which explains this curiosity and one should keep in mind that the range of viscosities is rather limited in this case.

5.5. *Free-surface vorticity*

It is well known that a drop coalescing with a flat liquid surface, or impacting onto it at low velocity, will produce a robust vortex ring which travels into the bottom layer, see e.g. Rogers (1858), Thomson & Newall (1885), Dooley *et al.* (1997) and the vorticity evolution studied by Peck & Sigurdson (1994). The vorticity in the ring is produced by the flow along a curved free surface, which produces vorticity at the free surface (Cresswell & Morton 1995). Heuristically, this occurs because irrotationality and the shear-free boundary conditions cannot both be satisfied at the curved surface and to avoid infinite accelerations irrotationality must be relaxed. This vorticity diffuses into a thin layer which may separate from the free surface, thus
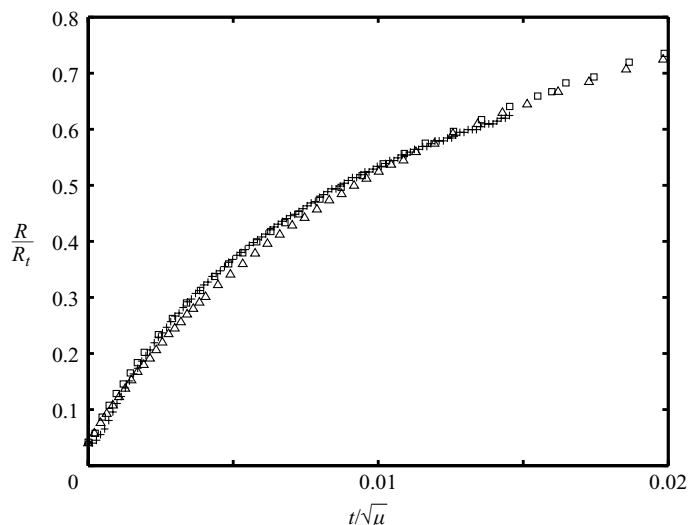
FIGURE 26. The data from figure 17(*b*), using the same symbols, where the time-axis has been divided by $\sqrt{\mu}$.
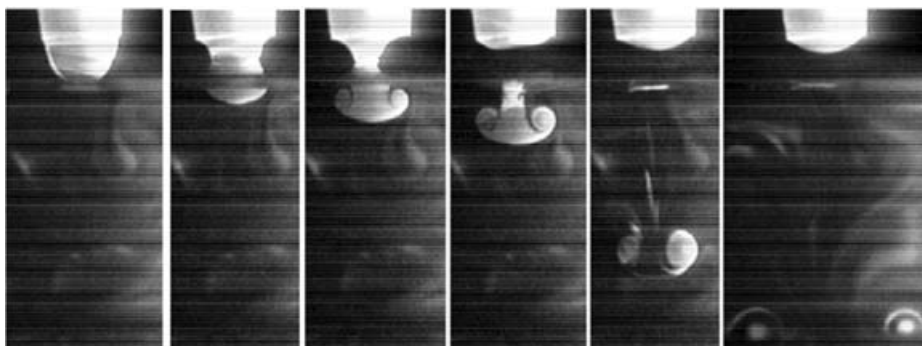

FIGURE 27. Coalescence of a dyed water drop with a flat liquid pool, which generates a vortex ring. The liquid is water and the nozzle opening is about 5 mm in diameter. The ring expands in the last panel, as it encounters the bottom of the tank.

entering the bulk liquid, see figure 27 as an example. This mechanism is absent in all of the inviscid theories describing coalescence, as they assume potential flow.

The symmetry of coalescing drops suggests the formation of two opposite sign vorticity layers, which might separate from the two sharp corners (figure 20) which form during the low-viscosity coalescence. If these vortex sheets separate, they would most probably produce an unstable configuration of two parallel vortex sheets of opposite sign, which could annihilate or wrap around one another.

Separation of the vorticity seems most likely if one drop is much larger than the other, as the internal pressure is then higher in the smaller drop, which promotes mean flow along the free surface, from the smaller to the larger drop. Photographs of this phenomena are shown in the above-cited papers and in Anilkumar, Lee & Wang (1991). The present experiments were not set up to identify such rings. However, were a vortex ring produced, one should expect the outwards motion of the neck region to slow down. Principally, because the energy released from the free surface would have

to go into the kinetic energy of the vortex ring in addition to increasing the added mass of the outward coalescence motion, e.g. discussion in Rein (2002). Our results, shown in figure 15, however, do not show any significant reduction in the value of C as the two tip radii of curvature become widely different, thus approaching the drop/pool configuration. For the largest difference in the two drop radii, the value of C reduces only by about 6%. This may suggest that vorticity layers are indeed formed even for the coalescence of equal sized drops, thus always absorbing some of the released surface energy. However, these vorticity layers may not separate from the free surface, or most probably not roll up to form coherent rings.

5.6. *Spherical drops*

For two perfectly spherical drops, we can predict analytically the speed of the outwards motion of the neck region based on (3.7). Here we know the form of $\delta(R)$ in the equation. Denoting the distance from the middle plane to the drop surfaces by δ_1 and δ_2, we obtain

$$\delta(R) = \delta_1 + \delta_2 = R_t + R_b - \sqrt{R_t^2 - R^2} - \sqrt{R_b^2 - R^2}.$$

Without loss of generality we set $R_t = 1$ and $R_b = \eta R_t$, i.e. we measure R in units of R_t, which gives

$$\frac{\delta}{R_t} = \delta^*(R) = 1 + \eta - \sqrt{1 - R^2} - \sqrt{\eta^2 - R^2},$$

which can be substituted into (3.7) and solved numerically.

For drops of identical radius $\eta = 1$ we obtain

$$v(R) = \frac{\mathrm{d}R}{\mathrm{d}t} = C\sqrt{\frac{\sigma}{2\rho}}\left(\frac{1}{1 - \sqrt{1 - R^2}} - \frac{2}{R}\right)^{1/2}, \tag{5.4}$$

which can be solved numerically for the appropriate initial conditions.

For tip radii of curvature smaller than the capillary length $R_{ave} < a$, the deformations of the drop shapes are small and the tip radii can be estimated by the overall radii of the drops, e.g. by half the horizontal width. The predicted motions from using (3.7) and (5.4) should then be the same.

6. Conclusions

We have measured the early surface motions during the coalescence of a pendent and a sessile drop. A dimensional model based on the vertical separation distance between the liquid surfaces has successfully described these motions up to $R/R_d \simeq 0.7$. This model, in (3.7), contains one empirical constant which takes a value of $C = 0.80 \pm 0.05$. This value of the non-dimensional coefficient C is similar to the value obtained by Thoroddsen *et al.* (2003) for the contraction of a thin disk of air caught under an impacting water drop. That study found a value of $C = 0.94$. The model used therein differs slightly from the present one, in that it only included one of the principal radii of curvature. Including the other radius of curvature, which has the same sign for an air disk, would lower the value of C to approximately 0.90 making its value even closer for the two configurations.

The coalescence motions were compared to power-law scalings. Reasonable agreement was found with the $R \propto t^{0.5}$ predictions of Eggers *et al.* (1999), for the early coalescence when $R/R_{ave} < 0.35$. In this region, we find a power coefficient of 0.46. This lower value of the coefficient might be caused by the finite initial contact

radius. For larger radii, the power-law slope becomes 0.41, significantly lower than the prediction, but in good agreement with earlier measurements of Menchaca-Rocha *et al.* (2001) for two sessile mercury drops.

The coalescence motions start at 20–50 µs after onset of electrical contact. We speculate that this hesitation may be caused partly by the entrapment of a minute disk of air at the centre of the contact. The contraction of this disk into a bubble will resist the outwards motion for the first few micro-seconds. The exact duration of this effect would depend on the initial thickness of this air disk, which could not be measured in our set-up. We also discuss other possible effects during the initial contact.

Experiments with drops of higher viscosity, by using glycerin/water mixtures, show a decrease in coalescence speed for $Re_v = \rho R_{ave} \sigma / \mu^2 < 5000$. This suggests that for water drops, the viscous forces only begin to affect the coalescence if their radii are smaller than 70 µm. This predicts capillary–inertial motions at scales of relevance to typical dimensions of MEMS devices, e.g. Velev, Prevo & Bhatt (2003). This drop size is consistent with the smallest droplets observed by Thoroddsen & Takehara (2000) in the capillary–inertial coalescence cascade, where a 180 µm drop has been observed to eject at high speed a 90 µm diameter satellite droplet. At $Re \sim 50$ the value of C has reduced by half, which corresponds to a water drop of only 2 µm in diameter.

As the viscosity is increased, the curvature in the neck region also becomes sharper and the shape changes qualitatively. This is quantified and is found to be consistent with earlier theoretical studies.

REFERENCES

ANILKUMAR, A. V., LEE, C. P. & WANG, T. G. 1991 Surface-tension-induced mixing following coalescence of initially stationary drops. *Phys. Fluids* A **3**, 2587–2591.

CHARLES, G. E. & MASON, S. G. 1960 The coalescence of liquid drops with flat liquid/liquid interfaces. *J. Colloid Sci.* **15**, 236.

CRESSWELL, R. W. & MORTON, B. R. 1995 Drop-formed vortex rings – The generation of vorticity. *Phys. Fluids* **7**, 1363.

DOOLEY, B. S., WARNCKE, A. E., GHARIB, M. & TRYGGVASON, G. 1997 Vortex ring generation due to the coalescence of a water drop at a free surface. *Exps. Fluids* **22**, 369–374.

DUCHEMIN, L., EGGERS, J. & JOSSERAND, C. 2003 Inviscid coalescence of drops. *J. Fluid Mech.* **487**, 167–178.

EGGERS, J. 1997 Nonlinear dynamics and breakup of free-surface flows. *Rev. Mod. Phys.* **69**, 865.

EGGERS, J., LISTER, J. R. & STONE, H. A. 1999 Coalescence of liquid drops. *J. Fluid Mech.* **401**, 293–310.

ETOH, T. G., POGGEMANN, D., RUCKELSHAUSEN, A. *et al.* 2002 A CCD image sensor of 1 M frames/s for continuous image capturing of 103 frames. *2002 IEEE Intl Solid-State Circuits Conf. Digest of Technical Papers, Visuals Supplement, 30–31,* vol. 386, pp. 46–47.

ETOH, T. G., POGGEMANN, D., KREIDER, G. *et al.* 2003 An image sensor which captures 100 consecutive frames at 1 000 000 frames/s. *IEEE Trans. on Electron Devices,* vol. 50, 144–151.

FORDHAM, S. 1948 On the calculation of surface tension from measurements of pendant drops. *Proc. R. Soc.* A **194** no. 3, pp. 1–16.

HOPPER, R. W. 1990 Plane Stokes flow driven by capillarity on a free surface. *J. Fluid Mech.* **213**, 349–375.

HOPPER, R. W. 1992 Stokes flow of a cylinder and a half-space driven by capillarity. *J. Fluid Mech.* **243**, 171–181.

HOPPER, R. W. 1993a Coalescence of two viscous cylinders by capillarity: Part I. Theory. *J. Am. Ceram. Soc.* **76**, 2947–2952.

HOPPER, R. W. 1993b Coalescence of two viscous cylinders by capillarity: Part II. Shape evolution. *J. Am. Ceram. Soc.* **76**, 2953–2960.

JONES, A. F. & WILSON, S. D. R. 1978 The film drainage problem in droplet coalescence. *J. Fluid Mech.* **87**, 263–288.

KELLER, J. B. & MIKSIS, M. 1983 Surface tension driven flows. *SIAM J. Appl. Maths* **43**, 268–277.

KELLER, J. B., MILEWSKI, P. A. & VANDEN-BROECK, J.-M. 2000 Merging and wetting driven by surface tension. *Eur. J. Mech.* B/*Fluids* **19**, 491–502.

KELLER, J. B., MILEWSKI, P. A. & VANDEN-BROECK, J.-M. 2003 Breaking and merging of liquid sheets and filaments. *J. Engng. Maths* **42**, 283–290.

LEE, J. G., MORI, H. & YASUDA, Y. 2002 Alloy phase formation in nanometer-sized particles in the In-Sn System. *Phys. Rev.* B **65**, paper 132106-1-4.

MARTINEZ-HERRERA, J. I. & DERBY, J. J. 1995 Viscous sintering of spherical particles via finite element analysis. *J. Am. Ceram. Soc.* **78**, 645–649.

MIKSIS, M. J. & VANDEN-BROECK J.-M. 1999 Self-similar dynamics of a viscous wedge of fluid. *Phys. Fluids* **11**, 3227–3231.

MENCHACA-ROCHA, A., MARTINEZ-DAVALOS, A., NUNEZ, R., POPINET, S. & ZALESKI, S. 2001 Coalescence of liquid drops by surface tension. *Phys. Rev.* E **63**, paper 046309, pp. 1–5.

OGUZ, H. N. & PROSPERETTI, A. 1989 Surface-tension effects in the contact of liquid surfaces. *J. Fluid Mech.* **203**, 149–171.

PECK, B. & SIGURDSON, L. 1994 The three-dimensional vortex structure of an impacting water drop. *Phys. Fluids* **6**, 564–576.

REIN, M. 2002 Capillary effects at newly formed liquid–liquid contacts. *Phys. Fluids* **14**, 411–414.

RICHARDSON, S. 1992 Two-dimensional slow viscous flows with time-dependent free boundaries driven by surface tension. *Eur. J. Appl. Maths* **3**, 193–207.

ROGERS, W. B. 1858 On the formation of rotating rings by air and liquids under certain conditions of discharge. *Am. J. Sci. Arts (Second Ser.)*, **26**, 246–258.

ROTHER, M. A., ZINCHENKO, A. Z. & DAVIS, R. H. 1997 Buoyancy-driven coalescence of slightly deformable drops. *J. Fluid Mech.* **346**, 117–148.

SHI, X. D., BRENNER, M. P. & NAGEL, R. S. 1994 A Cascade of structure in a drop falling from a faucet. *Science* **265**, 219–222.

STOVER, R. L., TOBIAS, C. W. & DENN, M. M. 1997 Bubble coalescence dynamics. *AIChE J.* **43**, 2385–2392.

THOMSON, J. J. & NEWALL, H. F. 1885 On the formation of vortex rings by drops falling into liquids, and some allied phenomena. *Proc. R. Soc. Lond.* **39**, 417–436.

THORODDSEN, S. T., ETOH, T. G. & TAKEHARA, K. 2003 Air entrapment under an impacting drop *J. Fluid Mech.* **478**, 125–134.

THORODDSEN, S. T. & TAKEHARA, K. 2000 The coalescence-cascade of a drop. *Phys. Fluids* **12**, 1265–1267.

VELEV, O. D., PREVO, B. G. & BHATT, K. H. 2003 On-chip manipulation of free droplets. *Nature* **426**, 515–516.

WU, M., CUBAUD, T., HO, C.-M. *et al.* 2003 Coalescence of liquid droplets in micro fluidic device. *Bull. APS* **48**, 224 (abstract only).

WU, M., CUBAUD, T. & HO, C.-M. 2004 Scaling law in liquid drop coalescence driven by surface tension. *Phys. Fluids* **16** (7), L51–L54.

ZEFF, B. W., KLEBER, B., FINEBERG, J. & LATHROP, D. P. 2000 Singularity dynamics in curvature collapse and jet eruption on a fluid surface. *Nature* **403**, 401–404.